Electronic Supplementary Material (ESI) for Journal of Materials Chemistry A.

Electronic Supplementary Information (ESI)

The Controlled Construction for Ternary Hybrid of Monodisperse Ni_3S_4 Nanorods/Graphitic C_3N_4 Nanosheets/Nitrogen-Doped Graphene in van der Waals Heterojunctions as Highly Efficient Electrocatalyst for Overall Water Splitting and a Promising Anode Material for Sodium-Ion Batteries

Jing Yang,[abcd] Shiqi Xing,[abcd] Jianbin Zhou,[abcd] Yun Cheng,[abcd] Lei Shi[de] and Qing Yang[abcd]*

[a] Hefei National Laboratory of Physical Sciences at the Microscale, University of Science and Technology of China (USTC), Hefei 230026, Anhui, P. R. China.

[b] Department of Chemistry, USTC, Hefei 230026, Anhui, P. R. China.

[c] Laboratory of Nanomaterials for Energy Conversion, USTC, Hefei 230026, Anhui, P. R. China.

[d] Synergetic Innovation Center of Quantum Information & Quantum Physics, USTC, Hefei 230026, Anhui, P. R. China.

[e] Hefei Science Center of CAS, University of Science and Technology of China, Hefei 230026, China.

* Corresponding author. E-mail: qyoung@ustc.edu.cn; Fax: +86-551-63606266; Tel: +86-551-63600243.

Experimental Section

1. Materials.

Nickel(II) acetylacetonate (hydrate) [95%, $Ni(acac)_2·xH_2O$] was purchased from TCI, 1-octanethiol [OTT, 98%] and oleylamine (OAm, 80%-90%) were obtained from Alfa Aesar. Nafion solution (5 wt%) was obtained from Sigma-Aldrich. Urea, graphite powder and solvents of toluene and isopropanol were purchased from

Sinopharm Chemical Reagent Ltd. Nickel foam was commercially available in different chemical reagent companies with similar performances. All reagents used as received in our experiments without any purification.

2. Synthesis of monodisperse Ni_3S_4 nanorods (m-Ni_3S_4 NRs).

In a typical procedure, 0.2 mmol (51.4 mg) nickel(II) acetylacetonate (hydrate) and 0.4 mL 1-octanethiol used as both Ni and S precursors, 5 mL oleylamine used as ligand and solvent, were all added into a 100-mL three-neck round-bottom flask. Under powerfully magnetic stirring and argon flow atmosphere, the flask was firstly heated to 120 °C and kept for 30 min under such condition to remove possible low-boiling point impurities besides dissolved oxygen and moisture. Subsequently, the equipment was further heated to 220 °C with a heating rate of 10 °C/min. After a facile one-pot reaction between precursor sources and OAm in this temperature for 60 min, the monodisperse uniform Ni_3S_4 nanorods were successfully synthesized. Finally, the black colloidal solution was cooled down to room temperature naturally. To get rid of the excess surfactants on the surface of Ni_3S_4 nanorods, the samples were washed with the mixed solvents of toluene and isopropanol for four times. The final product was dispersed in 1 mL toluene (20 mg mL^{-1}) for further use.

3. Synthesis of graphitic C_3N_4 nanosheets (g-C_3N_4 NS).

In a typical synthesis of g-C_3N_4 NS, urea was added into a quartz tube with a loose hat, and then, the quartz tube was placed in a tube furnace. With a heating rate of 5 °C/min, the tube was heated to 550 °C and kept in this condition for 5 h under flowing high-purity argon. After cooling down to room temperature naturally, the as-synthesized C_3N_4 was washed with deionized water for several times and dried in a vacuum oven at 70 °C for further use.

4. Fabrication for binary hybrid of monodisperse Ni_3S_4 nanorods/graphitic C_3N_4 nanosheets (m-Ni_3S_4 NRs/g-C_3N_4 NS).

The hybrid of m-Ni_3S_4 NRs/g-C_3N_4 NS was fabricaed through a solution-phase self-assembly strategy. Briefly, the as-synthesized Ni_3S_4 nanorods dispersed in 1 mL toluene (20 mg mL^{-1}) were added into 17 mL of toluene solution of g-C_3N_4 yellow powder (0.5 mg mL^{-1}) and the mixture was sonicated for 2 h in the surrounding environment, then the precipitate was collected by centrifuging and dried at 70 °C. To ensure stable in electrochemical testing, a heat treatment process was required at 250 °C under Ar flow for more than 2.5 h.

5. Synthesis of graphene oxide (GO).

The GO was easily synthesized by oxidizing natural graphite power through a modified Hummers' method.[1]

6. Synthesis of nitrogen-doped graphene (N-G).

5 mL of aqueous solution of urea (80 mg mL^{-1}) was added into 20 mL of aqueous solution of GO (0.5 mg mL^{-1}) under strong ultrasound conditions. After 30 min treatment, the homogenous mixture was obtained and transferred into a 30 mL Teflon-lined stainless steel autoclave and kept at 160 °C for 3 h. Then the black product was washed with deionized water and dried for further use.

7. Fabrication for binary hybrid of monodisperse Ni_3S_4 nanorods/nitrogen-doped graphene (m-Ni_3S_4 NRs/N-G).

The same strategy was performed as for the preparation of m-Ni_3S_4 NRs/g-C_3N_4 NS hybrid using Ni_3S_4 and N-G instead of Ni_3S_4 and C_3N_4.

8. Synthesis of graphitic C_3N_4 nanosheets/nitrogen-doped graphene (g-C_3N_4 NS/N-G) hybrid.

20 mL of aqueous solution of urea (80 mg mL^{-1}) was added into 80 mL of aqueous solution of GO (0.5 mg mL^{-1}) under strong ultrasound conditions. After 30 min, the uniform suspension was kept at 80 °C and constantly stirred by a magnetic stirrer until the water was removed absolutely, then put it into a vacuum oven (70 °C) overnight. Grinded the intermedium (GO/urea) into powder and added it into a quartz tube with a loose hat, then the quartz tube was placed in a tube furnace. The g-C_3N_4 NS/N-G hybrids were obtained after a heat treatment process at 550 °C for 2.5 h with a heating rate of 10 °C min^{-1} under Ar flow.

9. Fabrication for ternary hybrid of monodisperse Ni_3S_4 nanorods/graphitic C_3N_4

nanosheets/nitrogen-doped graphene (m-Ni_3S_4 NRs/g-C_3N_4 NS/N-G).

The same strategy was performed as for the preparation of m-Ni_3S_4 NRs/g-C_3N_4 NS hybrid using Ni_3S_4 and g-C_3N_4 NS/N-G instead of Ni_3S_4 and C_3N_4. A heat treatment at 250 °C under flowing argon for more than 2.5 h was also required to enhance the electrochemical properties of final m-Ni_3S_4 NRs/g-C_3N_4 NS/N-G hybrid.

A comparison of synthetic method in addition to phase and morphology of Ni_3S_4 between the reports in literature and current work was reviewed and collected in the following table (Table S1). As we know, Ni_3S_4 as the mineral polydymite existing in nature is not easy to be synthesized in the laboratory. It always appears along with some impurities like NiS_2 and/or NiS, as the studies reported in literature including refs. 5, 11, 13 and 16 in Table S1. To exclude these extra components (NiS_2 and/or NiS) from the targeting metastable phase of Ni_3S_4 and make the structure comparably stabilized, abundant explicit composites (consist of the predominant Ni_3S_4 products just with coexisted supporting matrixes) were widely investigated and developed by many groups via various synthetic procedures. For instance, the Ni_3S_4@C composite with hollow microspheres morphology was constructed through a hydrothermal route with a subsequent annealing procedure (RSC Adv., 2016, 6, 101752–101759). The Ni_3S_4-MoS_2 composite possessing core-nanosheets structure was fabricated by employing a hydrothermal approach (J. Mater. Chem. A, 2017, 5, 11278–11285), the blocky-like Ni_3S_4 particles with 1–2 μm in size located on the surface of FTO was obtained via a hydrothermal method (Electrochim. Acta, 2015, 170, 39–47), and the composite of PAN@CuS@Ni_3S_4 displaying a nanosheets-like geometry was finally received after a solvothermal process (Chem. Sel., 2016, 1, 3618–3622). Meanwhile, by using a piece of Ni foam as Ni-precursor source, hydrothermal sulfidation of this substrate is also a novel strategy to acquire the Ni_3S_4/Ni foam composites that with stacked nanosheets or nanosphere configurations (Chem. Eng. J., 2018, 343, 572–582; ACS Sustainable Chem. Eng., 2017, 5, 7203–7210). In general, the above mentioned products were respectively listed in Table S1 as refs. 4, 9, 12, 15, 2 and 7, showing excellent properties in the corresponding fields. To thoroughly explore the particular characteristics and potential applications of the pure Ni_3S_4 via reducing the inevitable interferences within the concomitant system, the monomorphic and pure Ni_3S_4 gradually attracts great attention and there have been many more efforts devoted to the syntheses of pure Ni_3S_4 in spite of the samples with large size and/or complicated preparation methods. Typically, an irregular Ni_3S_4 microsphere with a large size of 2 μm was reported in Chem. Lett., 2004, 33, 1294–1295 (ref. 17), the pure Ni_3S_4 consisting of thick and large flat sheets/sheet frames (130/160 nm) was synthesized in RSC Adv., 2015, 5, 8422–8426 (ref. 6), and the Ni_3S_4 nanoplates with 120–200 nm in length were fabricated in Mater. Lett., 2005, 59, 3728–3731 (ref. 14). In addition, spherical Ni_3S_4 exhibiting as large as 5 μm in diameter was also synthesized in J. Alloy Compd., 2015, 620, 42–47 (ref. 3). Although the Ni_3S_4 nanorods and nanoprisms/tetrahedrons with reduced sizes of 40 nm and 40/16 nm were obtained in ACS Nano 2018, 12, 1829–1836 (ref. 8) and Nanoscale, 2014, 6, 8935–8942 (ref. 10), respectively, both of them required a multiple-step synthetic route via additional hot-solution injections of S-precursor source into the complicated reaction system.

To simply the synthetic procedure, we develop a one-step colloidal route by using soluble $Ni(acac)_2$ and OTT as the precursors for the first time to reduce and simply the manipulations of the synthesis. Typically, the mixtures including Ni- and S-precursor sources as well as the solvent were all added into a flask one time at the beginning without any subsequent treatments during the reaction. This route could simplify the preparation with reduced apparatus and also reduce the production cost in a great degree, from which the obtained Ni_3S_4 nanorods are highly purified and monodispersed, show uniform shape and ultrasmall size of 40 nm in length and evenly distribute without any agglomeration in a large scale (Fig. 1a to 1c for detail information). That is to say, different from the reported literature mentioned above, we could simultaneously insure the optimal morphology and simplify the synthetic route as in the preparation of Ni_3S_4. As we know, the geometries and morphologies besides structures could significantly affect the electrochemical properties of samples, and the preparation methods could also impact the efficiency of manufacture while in practical applications. Thus, it is great potential for the products fabricated in the present route as a kind of substituted functional nanomaterials in the area of energy conversion and storage.

Most importantly, to enhance the stability, ameliorate the electroconductivity and make full use of functionalities of pure Ni_3S_4, a ternary hybrid of m-Ni_3S_4 NRs/g-C_3N_4 NS/N-G was constructed via a solution-phase self-assembly strategy in the present work for the first time. Typically, the active material of the Ni_3S_4 nanorods was wrapped by graphitic C_3N_4 nanosheets over the conducting substrate of nitrogen-doped graphene to enhance the corresponding functionalities (Fig. 1j to 1l) since the m-Ni_3S_4 NRs/g-C_3N_4 NS/N-G with robust and intertwined nanostructures could shorten the diffusion pathways, decrease the diffusion resistance and accelerate the transfer speed of electrons and ions. In addition, this kind of composite architecture constructed by van der Waals heterojunctions (resulted from the interaction of hydrophobic force between the three components, similar to the early report in literature as seen in refs. 8, 51–56 in main text) could also avoid the agglomeration, obscission, anisotropic volume expansion and irreversible mechanical failure of the active materials while in the electrochemical reactions. Particularly, the plentiful nano-scale pore-like and channel-like textures existed in the ternary hybrid could act as thoroughfares for expediting the transport of electrolyte to flood and interact with the reaction sites, dynamically and thermodynamically, which makes the hybrid delivers not only superior electrocatalytic hydrolysis properties but also excellent SIB performance in current work.

Table S1 A comparison including synthetic method in addition to phase and morphology of Ni_3S_4 between current work and investigations in reported literature.

No.	Phase	Morphology	Size	Synthetic method	References
1	pure Ni_3S_4	monodisperse uniform nanorods	40 nm in length	a simple one-pot colloidal synthetic procedure	this work
2	Ni_3S_4/Ni foam	stacked nanosheets	/	hydrothermal sulfidation of Ni foam substrate	Chem. Eng. J., 2018, 343, 572–582.
3	pure Ni_3S_4	spherical morphology	5 µm	thermal decomposition method	J Alloy Compd, 2015, 620, 42–47.
4	Ni_3S_4@C	hollow microspheres	1.5 µm	hydrothermal route and annealing treatment	RSC Adv., 2016, 6, 101752–101759
5	NiS/Ni_3S_4	hollow spheres	200 nm	hydrothermal method	J. Phys. Chem. C 2016, 120, 14581–14589.
6	pure Ni_3S_4	flat sheets/sheet frames	130/160 nm	solvothermal route	RSC Adv., 2015, 5, 8422–8426.
7	Ni_3S_4/Ni foam	nanosphere configuration	3-5 µm	hydrothermal-sulfurization strategy	ACS Sustainable Chem. Eng., 2017, 5, 7203–7210.
8	pure Ni_3S_4	nanorods	40 nm	an injection method	ACS Nano 2018, 12, 1829–1836.
9	Ni_3S_4-MoS_2	core-nanosheets	0.7 µm	hydrothermal approach	J. Mater. Chem. A, 2017, 5, 11278–11285.
10	pure Ni_3S_4	nanoprisms/tetrahedron	40/16 nm	hot injection method	Nanoscale, 2014, 6, 8935–8942.
11	Ni_3S_4 mixed with NiS	irregular particle shape	/	solventless thermal decomposition	Nano Lett., 2004, 4, 537–542.
12	Ni_3S_4/FTO	blocky-like particles	1-2 µm	hydrothermal method	Electrochim. Acta, 2015, 170, 39–47.
13	NiS/Ni_3S_4, $NiS_{1.03}$/Ni_3S_4	nanosheets/nanoneedles	large areas/1 µm	microemulsion-as-siste-d hydrothermal process	Chem. Lett., 2003, 32, 996, 996–997.
14	pure Ni_3S_4	nanoplates	120-200 nm	colloidal synthetic procedure	Mater. Lett., 2005, 59, 3728–3731
15	PAN@CuS@Ni_3S_4	nanosheets	/	solvothermal method	Chem. Sel., 2016, 1, 3618–3622.
16	Ni_3S_4/NiS_2, Ni_3S_4/NiS	rod-like morphology	15-50 µm	solvothermal process	Mater. Chem. Phys., 2002, 74, 230–233.
17	pure Ni_3S_4	irregular microspheres	2 µm	hydrothermal condition	Chem. Lett., 2004, 33, 1294–1295.

Structural characterization.

Structure analysis of the as-synthesized products was examined by X-ray powder diffraction (XRD) patterns which were carried out on a Philips X'pert PRO X-ray diffractometer with Cu-Kα radiation (λ = 1.54182 Å), while the morphological analysis of the as-synthesized products was acquired by a Hitachi (H7650) transmission electron microscope (TEM) operated at an acceleration voltage of 100 KV. In addition, the high resolution TEM (HRTEM), selected area electron diffraction (SAED) patterns, high-angle annular dark-field scanning transmission electron microscope (HAADF-STEM) and the corresponding energy-dispersive X-ray spectroscope (EDX) mapping analyses were executed on a JEOL JEM-ARF200F TEM/STEM with a spherical aberration corrector. To study the valences of the elements in as-synthesized products, X-ray photoelectron spectra (XPS) data were obtained using an ESCALAB 250 spectrometer (Perkin-Elmer) with a Kratos Analytical spectrometer and a monochromatic Al Kα (1486.6 eV) as the excitation source. The other structural information of products was revealed through attenuated total reflection Fourier transformed infrared (ATR-FTIR) spectra which were carried out in an ATR-FTIR spectroscopy (Prestige-21, SHIMADZU) at room temperature. Elemental analysis (ICP-AES) were performed by inductively coupled plasma atomic emission spectroscopy at Galbraith Laboratories (Knoxville, TN) and the Thermogravimetric analysis (TGA) was executed on a SDTQ600 (TA Instruments) TG-DTA Analyzer under different atmosphere.

Testing of electrocatalytic performance.

Because of serious agglomeration while Ni_3S_4 nanorods were dispersed in a mixed solution of water and ethanol, the preparation method of traditional glassy carbon electrode is not suitable for use in this work. Based on this phenomenon, nickel foam was used as a novel working electrode with excellent three-dimensional structures to explore the electrocatalytic performance of ternary hybrid of m-Ni_3S_4 NRs/g-C_3N_4 NS/N-G as well as other electrocatalysts. In detail, 100 uL increments of homogeneous final product solution (dispersed in 1 mL toluene with a concentration of 28.5 mg mL^{-1}) were evenly drip coated onto a 1 cm^2 piece of nickel foam, lead to an approximate m-Ni_3S_4 NRs/g-C_3N_4 NS/N-G catalyst loading ~2.8 mg cm^{-2}. After drying under ambient conditions, 100 uL increments of the diluted naphthol solution were then evenly drip coated onto the surface of above catalyst-decorated nickel foam to from a three-dimensional network, which could encapsulate the catalyst and prevent it falling from the electrode during electrochemical catalysis. Particularly, this two-step electrode preparation method could prevent the agglomeration of Ni_3S_4 catalyst while it coexists with naphthol in toluene solution. For comparison, m-Ni_3S_4 NRs/g-C_3N_4- and Ni_3S_4 NRs/N-G-decorated nickel foam working electrodes were also prepared in the same way.

An electrochemical workstation (CHI 660E) equipped with a three-electrode system was used to test the OER and HER electrochemical activities in 1 M KOH electrolyte at room temperature. A Pt electrode was served as counter electrode, an Ag/AgCl electrode was served as reference electrode and catalyst-modified nickel foam prepared according to the above steps was served as working electrode. All of the HER and OER reference electrodes in this article were transformed to reversible hydrogen electrodes (RHE) based on the equation of E (RHE) = E (Ag/AgCl) + 0.0592 pH + 0.197. As a test method, the cyclic voltammetry (CV) with a scan rate of 50 mV s^{-1} which could activate the electrode in the initial stage was measured by sweeping potential from 0 to –0.6 V versus the RHE for HER and from 1.2 to 1.7 V versus the RHE for OER. Meanwhile, the linear-sweep voltammetry (LSV) was also carried out at a sweep rate of 5 mV s^{-1} to reveal basic catalytic performance of the catalysts (the LSV of HER and OER displayed in this article were all obtained after iR-corrected). To investigate the electrocatalytic kinetic process, the electrochemical impedance spectroscopy (EIS) was obtained by using an amplitude of 5 mV under the frequency range from 100 kHz to 0.01 Hz. Additionally, overall water splitting in 1 M KOH was also explored in present work. The catalyst-modified Ni foam as cathode and the other one as anode were used to set up a testing system. Similar to HER and OER test, CV curves were recorded at a scan rate of 50 mV s^{-1} under the sweep potential from 1 to 2 V and LSV curves were recorded at a scan rate of 5 mV s^{-1} under the sweep potential from 1.1 to 2 V.

Sodium-ion battery (SIB) properties measurements.

Half cells (2016 R-type) were used to evaluate the sodium storage performance of as-synthesized products. After ball-milling for 4 h, the slurry which consisted of active materials, acetylene black and poly(vinyl difluoride) (PVDF, dispersed in the solution of N-methyl-2-pyrrolidone (NMP)) with a weight ratio of 80 : 10 : 10 was pasted onto a copper foil to form a working electrode. In order to remove the solvent and moisture contents existed in active materials, the copper foil was put into a vacuum oven and dried at 80 °C for 12 h. For SIB test, the coin cells were assembled in a glove box, using sodium foil as counter electrodes and a solution of sodium hexafluorophosphate ($NaPF_6$, 1.0 M) in diglyme (GIGLYME = 100 Vol%) as electrolyte, in addition, the counter and working electrode were separated by a Whatman glass fiber (GF/D) film. The galvanostatic charge/discharge performance of cells was analyzed on a LAND CT 2001A battery tester at different current densities with a voltage window from 0.01–3 V. The cyclic voltammetry (CV) curves of materials were carried out on a CHI 660E workstation at a scanning rate of 0.2 mV s^{-1} by sweeping the potential from 0.01 to 3 V, and electrochemical impedance spectroscopy (EIS) was also collected by this workstation in a frequency range from 100 kHz to 0.1 Hz. All the performances were tested at room temperature.

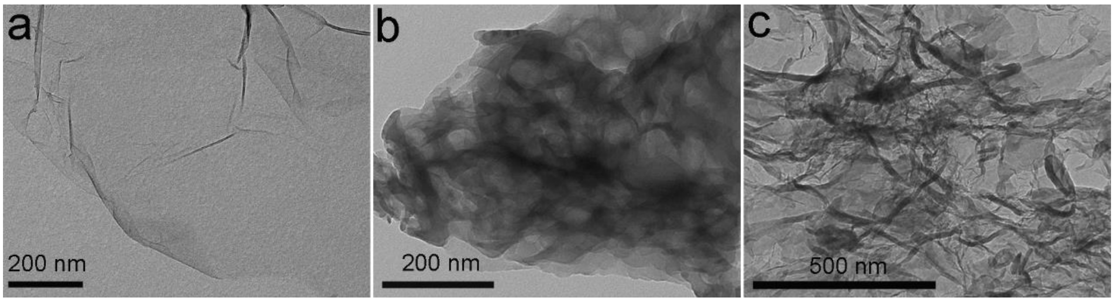

Fig. S1 TEM images of (a) pure N-G, (b) pure g-C_3N_4 NS and (c) g-C_3N_4 NS/N-G hybrids, respectively.

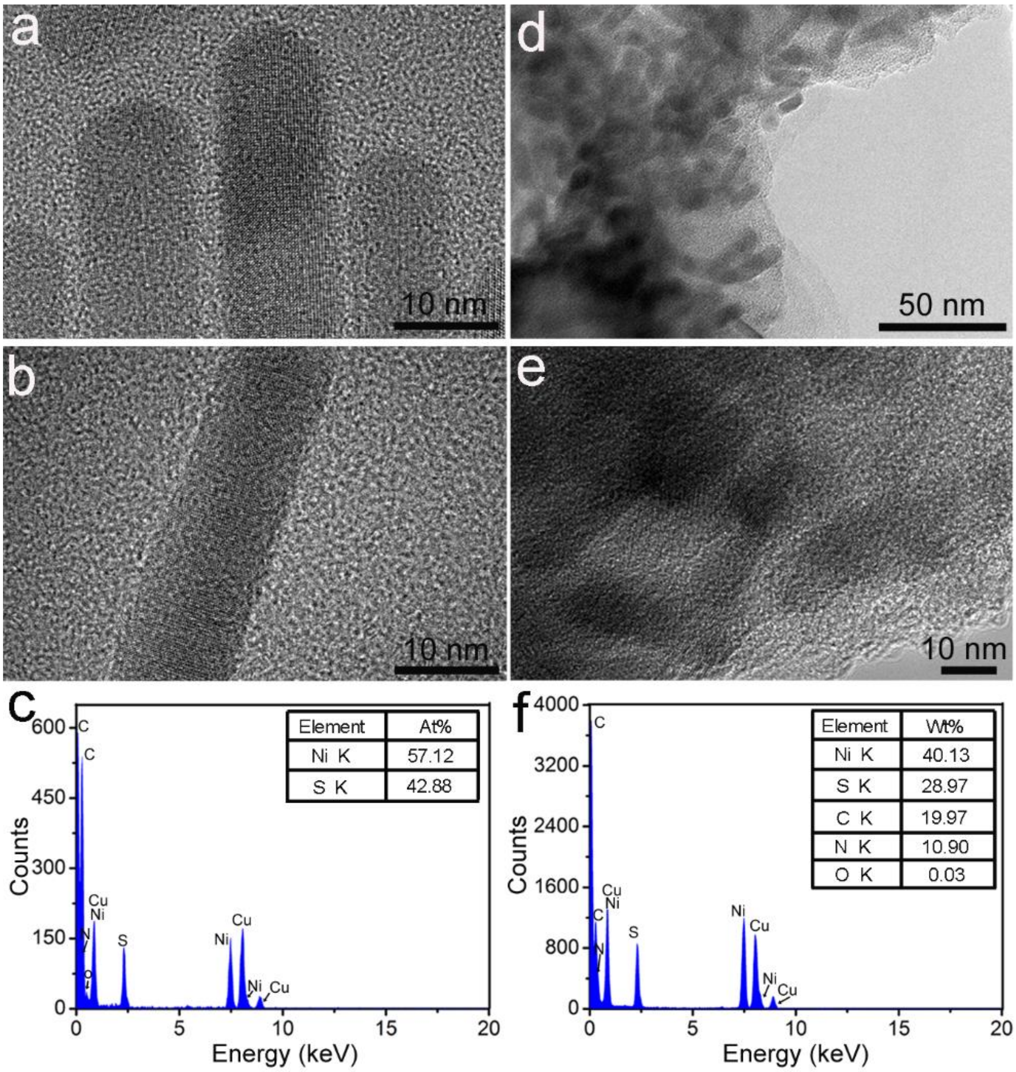

Fig. S2 Additional HRTEM images and EDX spectra for pure m-Ni_3S_4 NRs (a-c) and ternary hybrid of m-Ni_3S_4 NRs/g-C_3N_4 NS/N-G (d-f). The Cu signal in the spectra caused by the copper grid. The C signal in 2c resulted from carbon membrane which was coated on the copper grid, but in 2f from g-C_3N_4 NS/N-G matrix since we used microgrid during the measurement.

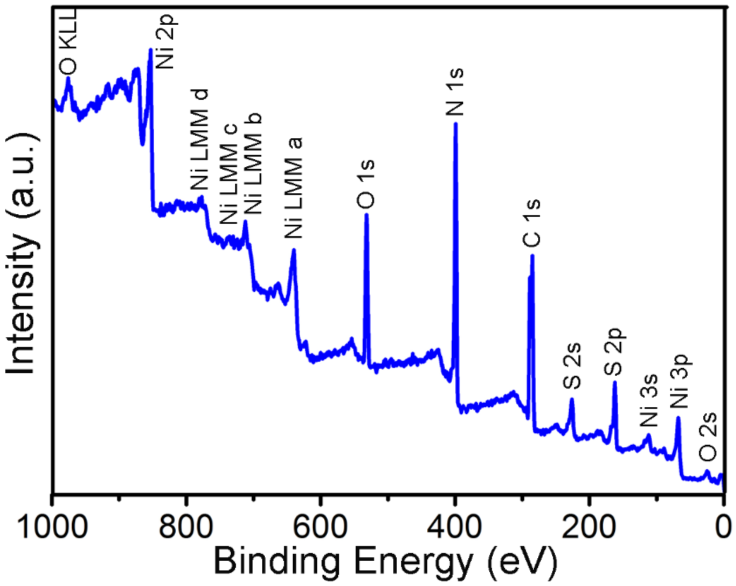

Fig. S3 The XPS survey spectra for ternary hybrid of m-Ni_3S_4 NRs/g-C_3N_4 NS/N-G.

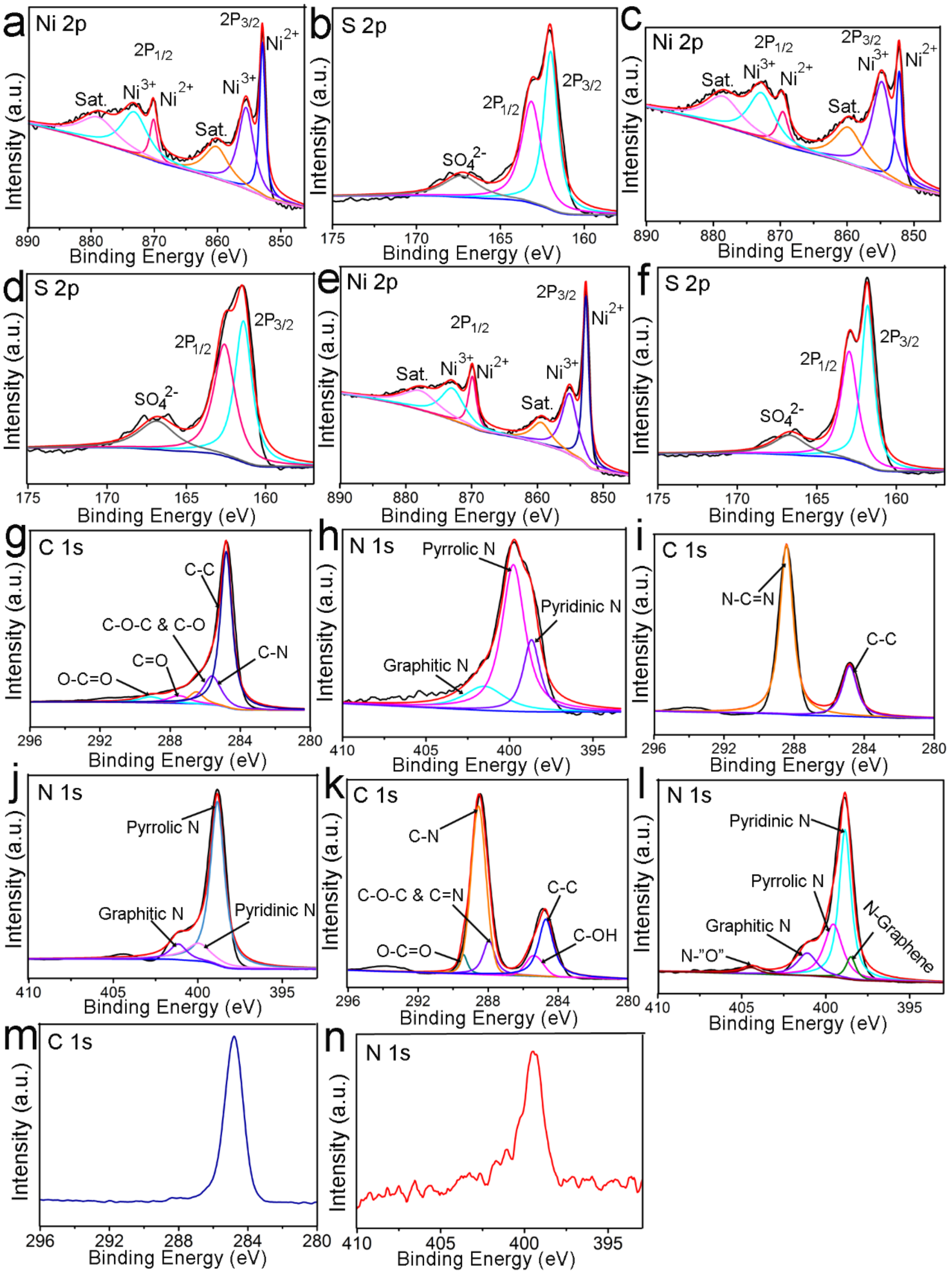

Fig. S4 High-resolution XPS spectra of (a) Ni 2p and (b) S 2p for m-Ni_3S_4 NRs/N-G hybrid; (c) Ni 2p and (d) S 2p for m-Ni_3S_4 NRs/g-C_3N_4 NS hybrid; (e) Ni 2p and (f) S 2p for pure m-Ni_3S_4 NR; (g) C 1s and (h) N 1s for pure N-G; (i) C 1s and (j) N 1s for pure g-C_3N_4 NS; (k) C 1s and (l) N 1s for g-C_3N_4 NS/N-G binary hybrid; and (m) C 1s and (n) N 1s for pure m-Ni_3S_4 NR.

ICP and TG measurements were carefully carried out to determine the weight ratio of individual components within the various hybrids developed in current work. In detail, for ICP, 10 mg product was dissolved in 5 mL solvent, and the concentrations of Ni and S elements could be accurately detected (Table S2). After an easy calculation, three similar weight percent values of 69.08%, 68.56% and 69.63% for Ni_3S_4 in the hybrids of m-Ni_3S_4 NRs/N-G, m-Ni_3S_4 NRs/g-C_3N_4 NS and m-Ni_3S_4 NRs/g-C_3N_4 NS/N-G are obtained, respectively, in close agreement with the initial proportion of individuals which were introduced into the mixed solutions before the self-assembly process, further suggesting the robust Van der Waals effects among three hybrids and the successful constructions of architectures with heterostructures. Based on this, it is feasible to compare the electro-catalytic properties and Na storage capacity on Ni_3S_4 among each composite.

In addition, TGA of the hybrids was displayed in Fig. S5 which could provide more evidence for the analysis mentioned above. As observed, the weight stepwise losing in air in a_1 (Fig. S5a, for ternary hybrid of m-Ni_3S_4 NRs/N-G), b_1 (Fig. S5b, for binary hybrid of m-Ni_3S_4 NRs/g-C_3N_4 NS) and c_1 stages (Fig. S5c, for binary hybrid of m-Ni_3S_4 NRs/g-C_3N_4 NS/N-G) are resulting from the removal of moisture at low temperature, and the evaporation of sulfur, the phase transformation from nickel sulfide to nickel oxide as well as the decomposition of g-C_3N_4 NS or/and N-G by an oxidation process while subsequently increasing the temperature of samples to a higher region.[2–4] Because of some overlaps among the above mentioned stages, it will lead a larger deviation while obtain the carbon content of composites by observing the weight loss from curves of TGA directly. To prevent this issue and simplify the analysis procedures, we calculated the mass percentages of m-Ni_3S_4 NRs within the three hybrids firstly by converting the corresponding content of final pure NiO remnants to Ni_3S_4. In general, the converted NiO was generated at 750 °C and has been accurately verified by the XRD patterns after TG tests, as shown in Fig. S5e. In detail, except for NiO (JCPDS:

01-073-1519), there are not any extra diffraction peaks appear in Fig. S5e, indicating the complete decomposition of carbon materials and all of the m-Ni_3S_4 NRs components were transferred to NiO eventually. In typical, the obtained NiO possesses weight percentages of 50.99%, 50.81% and 50.68% relative to that of initial m-Ni_3S_4 NRs/N-G, m-Ni_3S_4 NRs/g-C_3N_4 NS and m-Ni_3S_4 NRs/g-C_3N_4 NS/N-G, respectively, revealing that 69.25%, 69.01% and 68.83% (mass) of m-Ni_3S_4 NRs, as well as 30.75%, 30.99% and 31.17% (mass) of carbon substrate existed in the corresponding hybrids, which are consistent with the data detected by ICP analysis (Table S2).

Furthermore, the TG analysis of g-C_3N_4 NS/N-G hybrid detected in the N_2 atmosphere was also employed and depicted in Fig. S5d for the determination of N-G composition in the hybrid. In principle, the residuals above 750 °C for the g-C_3N_4 NS/N-G would be resulted from the existence of stable C species under inert conditions, that is to say, the content of N-G is approximately 31.07 wt% in g-C_3N_4 NS/N-G and 9.68 wt% in m-Ni_3S_4 NRs/g-C_3N_4 NS/N-G, respectively, due to the same preparation process of g-C_3N_4 NS/N-G in these two hybrids.[3–4] As a result, the concise information is summarized in Table S3. The weight ratio of m-Ni_3S_4 NRs : N-G in the m-Ni_3S_4 NRs/N-G hybrid is approximate 7 : 3, the weight ratio of m-Ni_3S_4 NRs : g-C_3N_4 NS in the m-Ni_3S_4 NRs/g-C_3N_4 NS hybrid is also approaching to 7 : 3, and the weight ratio of m-Ni_3S_4 NRs : N-G : g-C_3N_4 NS in the ternary hybrid of m-Ni_3S_4 NRs/g-C_3N_4 NS/N-G is very close to 7 : 2 : 1.

Table S2 ICP analyses of various hybrids in the present work.

Products	Concentration (ug/mL)		Weight percent of Ni_3S_4 (%)
	Ni	S	
m-Ni_3S_4 NRs/N-G	800.11	581.39	69.08
m-Ni_3S_4 NRs/g-C_3N_4 NS	795.32	575.89	68.56
m-Ni_3S_4 NRs/g-C_3N_4 NS/N-G	808.13	584.45	69.63

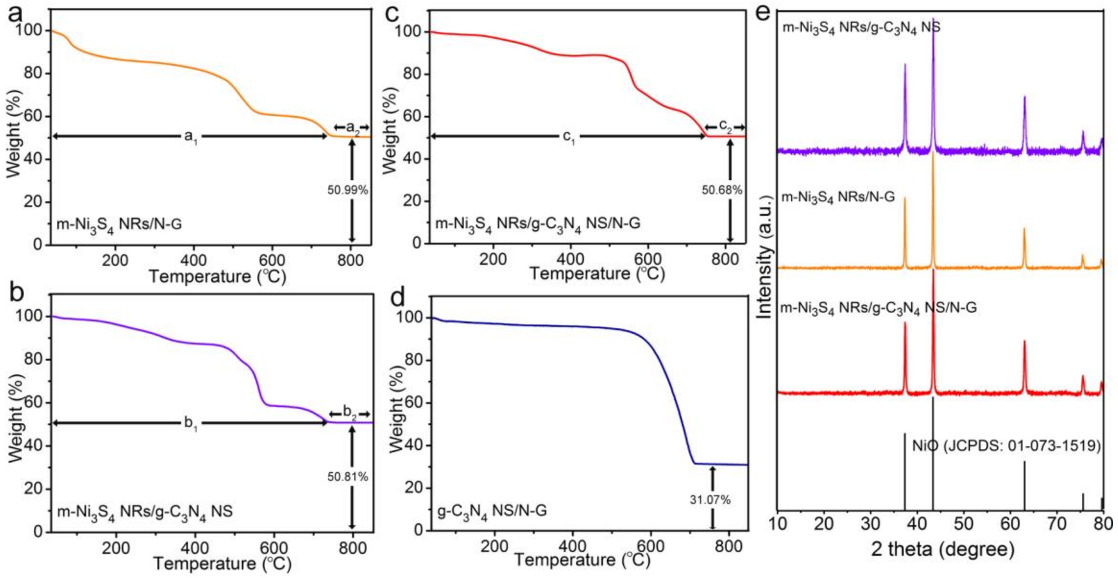

Fig. S5 TGA for hybrids of m-Ni_3S_4 NRs/N-G (a), m-Ni_3S_4 NRs/g-C_3N_4 NS (b) and m-Ni_3S_4 NRs/g-C_3N_4 NS/N-G (c) in air as well as the one of g-C_3N_4 NS/N-G hybrid in N_2 atmosphere (d). The XRD patterns of above three m-Ni_3S_4 NRs-based hybrids after TG texts (e).

Table S3 Weight ratio of individual components in m-Ni_3S_4 NRs-based hybrids.

Products	Weight percent (%)			weight ratio
	m-Ni_3S_4 NRs	g-C_3N_4 NS	N-G	
m-Ni_3S_4 NRs/N-G	69.25	/	30.75	Ni_3S_4 : N-G = 7 : 3
m-Ni_3S_4 NRs/g-C_3N_4 NS	69.01	30.99	/	Ni_3S_4 : g-C_3N_4 = 7 : 3
m-Ni_3S_4 NRs/g-C_3N_4 NS/N-G	68.83	21.49	9.68	Ni_3S_4 : g-C_3N_4 : N-G = 7 : 2 : 1

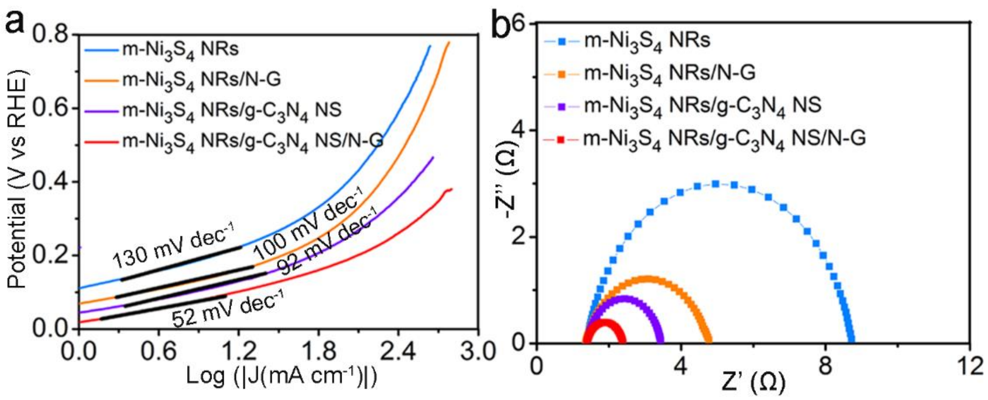

Fig. S6 (a) Tafel slopes for HER and (b) Nyquist plot (fitted using the modified Randles circuits) measured at η = 450 mV for OER.

Table S4 The HER activity comparison of m-Ni_3S_4 NRs/g-C_3N_4 NS/N-G ternary hybrid prepared in the current work with some typical nickel sulfide-based electrocatalysts recently reported.

Catalyst	Tafel slope (mV	η_{10} (mV)	Electrolyte	Reference
m-Ni_3S_4 NRs/g-C_3N_4 NS/N-G	52	95	1 M KOH	This work
Ni_xS/NF	90	113	1 M KOH	[5]
NiS_2	82	148	1 M KOH	[6]
NiS nanoparticles	124	474	1 M KOH	[7]
NiS_2 nanoparticles	128	454	1 M KOH	[7]
Ni_3S_2 nanoparticles	97	335	1 M KOH	[7]
NGO/Ni_7S_6	145.5	370	1 M KOH	[8]
Ni_3S_4/NF	69	122	1 M KOH	[9]
Ni_3S_2-NGQDs/NF	89	218	1 M KOH	[10]
Ni_3S_2/NF	138.3	274	1 M KOH	[10]

Table S5 The impedance parameters of the various catalysts in the present work.

Catalyst	**R_s (Ω)$_{(HER)}$**	**R_{ct} (Ω)$_{(HER)}$**	**R_s (Ω)$_{(OER)}$**	**R_{ct} (Ω)$_{(OER)}$**
m-Ni_3S_4 NRs/g-C_3N_4 NS/N-G	1.01	1.78	1.38	2.38
m-Ni_3S_4 NRs/g-C_3N_4 NS	1.03	3.13	1.40	3.43
m-Ni_3S_4 NRs/N-G	1.04	6.11	1.40	4.68
m-Ni_3S_4 NRs	1.06	8.93	1.42	8.72

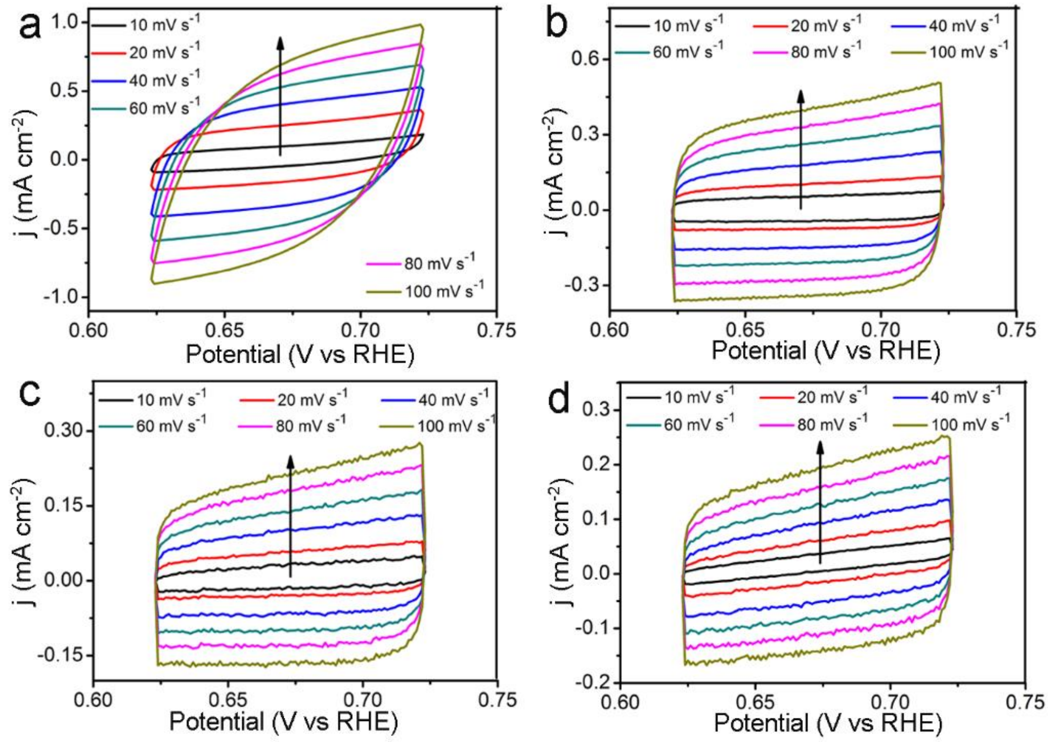

Fig. S7 Cyclic voltammetry curves of m-Ni_3S_4 NRs/g-C_3N_4 NS/N-G (a), m-Ni_3S_4 NRs/g-C_3N_4 NS (b), m-Ni_3S_4 NRs/N-G (c) hybrid and pure m-Ni_3S_4 NRs (d) in the region of 0.623-0.723 V vs. RHE.

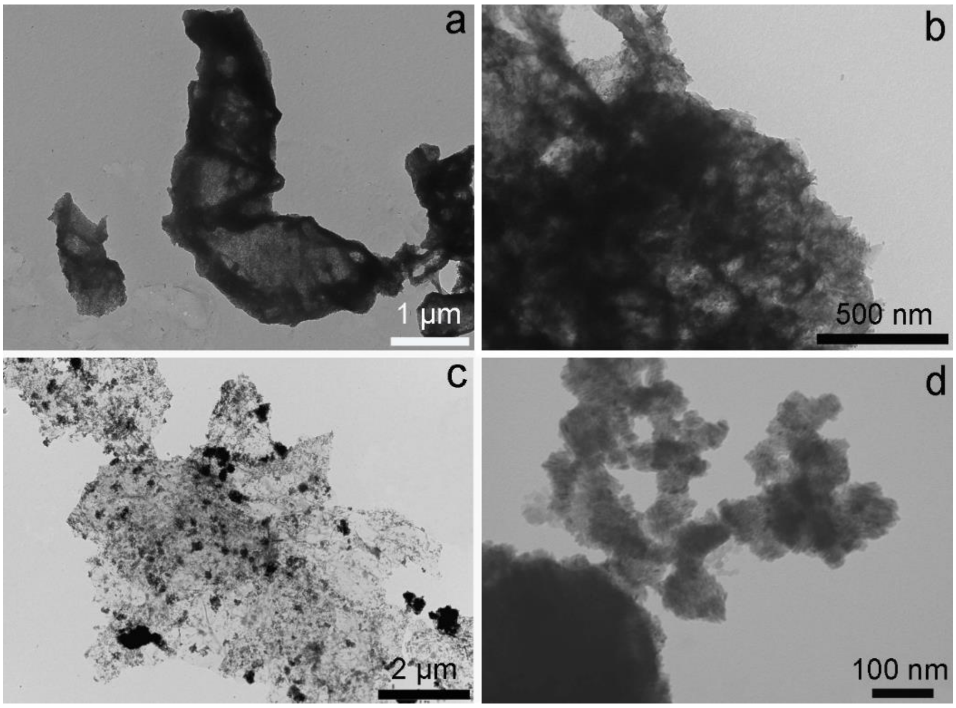

Fig. S8 TEM images of m-Ni_3S_4 NRs/g-C_3N_4 NS/N-G (a), m-Ni_3S_4 NRs/g-C_3N_4 NS (b), m-Ni_3S_4 NRs/N-G (c) hybrid and pure m-Ni_3S_4 NRs (d) after long term durability test.

We have carefully measured the electrocatalytic properties of pure g-C_3N_4 NS, pure N-G, hybrid of g-C_3N_4 NS/N-G, as well as the mechanical mixtures including g-C_3N_4 NS + N-G, m-Ni_3S_4 NRs + g-C_3N_4 NS, m-Ni_3S_4 NRs + g-C_3N_4 NS + N-G, m-Ni_3S_4 NRs + N-G and m-Ni_3S_4 NRs + g-C_3N_4 NS/N-G (the mechanical mixtures were obtained by grinding the corresponding various individual components which are in a same proportion as the hybrids based on the weight ratio detected in Table S3), the results were accurately summarized in Fig. S9 for further comparison. As estimated, in the absence of m-Ni_3S_4, the pure g-C_3N_4 NS, g-C_3N_4 NS + N-G mixtures, pure N-G and even g-C_3N_4 NS/N-G hybrid show negligible catalytic performance in the processes of HER (Figure Fig. S9a and b), OER (Fig. S9c and d) and overall water splitting (Fig. S9e and f). As a matter of fact, in current work, the catalytic active material is served by m-Ni_3S_4, while the g-C_3N_4 NS is an excellent matrix to hinder the agglomeration of active materials and achieve good dispersion of it, which could ensure substantial exposure of the active sites in m-Ni_3S_4. In detail, as obviously observed in Fig. S8, after long term durability test, there are not any changes detected in both m-Ni_3S_4 NRs/g-C_3N_4 NS/N-G and m-Ni_3S_4 NRs/g-C_3N4 NS, nevertheless, serious obscission and agglomeration of active materials are observed in the m-Ni_3S_4 NRs/N-G and pure m-Ni_3S_4 NRs. Based on this, the g-C_3N_4 NS corbelled materials of m-Ni_3S_4 NRs/g-C_3N_4 NS/N-G ternary hybrid and m-Ni_3S_4 NRs/g-C_3N_4 NS binary hybrid deliver satisfying C_{dl} values of 7.0 mF cm^{-2} and 3.5 mF cm^{-2}, respectively, higher than m-Ni_3S_4 NRs/N-G and pure m-Ni_3S_4 NRs of 1.7 mF cm^{-2} and 1.5 mF cm^{-2}, respectively (Fig. 5g). Therefore, it is confirmed that the moderate g-C_3N_4 NS is used as a robust substrate for active materials and it indeed plays an important role in ensuring a much more stable structure during the whole reactions to facilitate the catalysis of active m-Ni_3S_4 NRs in the electrolyte. In addition to the appropriate introduction of N-G which immensely improves the electrical conductivity of materials as we know, the ternary hybrid of m-Ni_3S_4 NRs/g-C_3N_4 NS/N-G displays superior electrochemical performance in this work.

Moreover, it is interesting to find that there is the same electrocatalytic activity sequence for the catalysts in all of the HER, OER and overall water splitting processes: blank electrode < g-C_3N_4 NS < g-C_3N_4 NS + N-G < N-G < g-C_3N_4 NS/N-G < m-Ni_3S_4 NRs + g-C_3N_4 NS < m-Ni_3S_4 NRs + g-C_3N_4 NS + N-G < m-Ni_3S_4 NRs + N-G < m-Ni_3S_4 NRs + g-C_3N_4 NS/N-G < m-Ni_3S_4 NRs < m-Ni_3S_4 NRs/N-G < m-Ni_3S_4 NRs/g-C_3N_4 NS < m-Ni_3S_4 NRs/g-C_3N_4 NS/N-G. Typically, the hybrid of g-C_3N_4 NS/N-G exhibits better hydrolysis activities than the corresponding pure individuals of g-C_3N_4 NS and N-G as well as the mechanical mixture of g-C_3N_4 NS + N-G, which suggests the significant synergistic effect in the hybrid of g-C_3N_4 NS/N-G. Similarly, as for other materials which with the participation of m-Ni_3S_4 NRs, the hybrids always present superior water splitting performance while the corresponding individuals and mechanical mixtures do not perform satisfactorily. In detail, the HER, OER and overall water splitting activities of m-Ni_3S_4 NRs/N-G hybrid are obviously better than pure m-Ni_3S_4 NRs, pure N-G and the m-Ni_3S_4 NRs + N-G mixtures. Meanwhile, the activities of m-Ni_3S_4 NRs/g-C_3N_4 NS hybrid are better than pure m-Ni_3S_4 NRs, pure g-C_3N_4 NS and the m-Ni_3S_4 NRs + g-C_3N_4 NS mixtures. Moreover, the activities of m-Ni_3S_4 NRs/g-C_3N_4 NS/N-G hybrid are better than pure m-Ni_3S_4 NRs, g-C_3N_4 NS/N-G and the m-Ni_3S_4 NRs + g-C_3N_4 NS/N-G mixtures while the activities of m-Ni_3S_4 NRs + g-C_3N_4 NS/N-G are better than m-Ni_3S_4 NRs + g-C_3N_4/NS + N-G mixtures. Based on the working mechanism summarized in the article, the difference of catalytic activities between hybrids, pure individuals and corresponding mechanical mixtures is mainly caused by the newly generated electrochemical reactive sites, stabilized structures, enhanced conductivity, as well as the synergistic and link-coupled effects among the two/three components in the binary/ternary hybrids, which certainly derive from the integrated process via van der Waals interactions. From the results analyzed above, it is no doubt that the hybrids of g-C_3N_4 NS/N-G, m-Ni_3S_4 NRs/N-G, m-Ni_3S_4 NRs/g-C_3N_4 NS and m-Ni_3S_4 NRs/g-C_3N_4 NS/N-G are indeed consisted by van der

Waals heterojunctions due to the interaction of hydrophobic force between the three components in the hybrid.

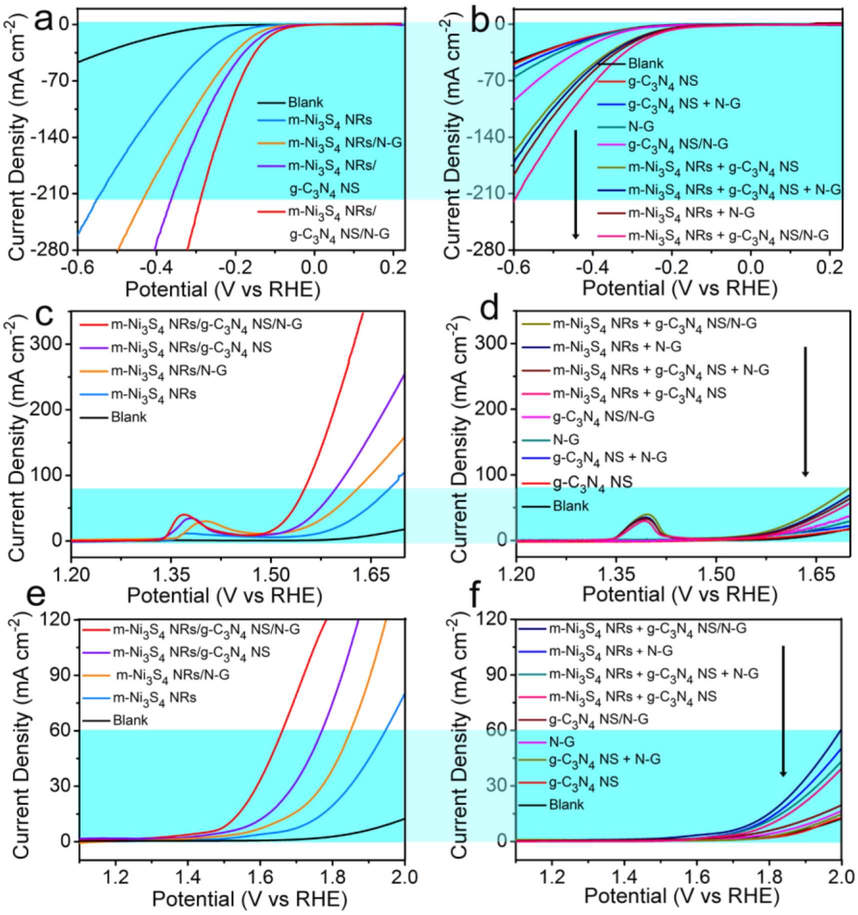

Fig. S9 HER (a), OER (c) and overall water splitting (e) performance for blank electrode, m-Ni_3S_4 NRs, m-Ni_3S_4 NRs/N-G, m-Ni_3S_4 NRs/g-C_3N_4 NS and m-Ni_3S_4 NRs/g-C_3N_4 NS/N-G. For further comparison, the HER (b), OER (d) and overall water splitting (f) performance for the g-C_3N_4 NS, N-G, g-C_3N_4 NS/N-G and corresponding mechanical mixtures including g-C_3N_4 NS + N-G, m-Ni_3S_4 NRs + g-C_3N_4 NS, m-Ni_3S_4 NRs + g-C_3N_4 NS + N-G, m-Ni_3S_4 NRs + N-G and m-Ni_3S_4 NRs + g-C_3N_4 NS/N-G were subsequently measured.

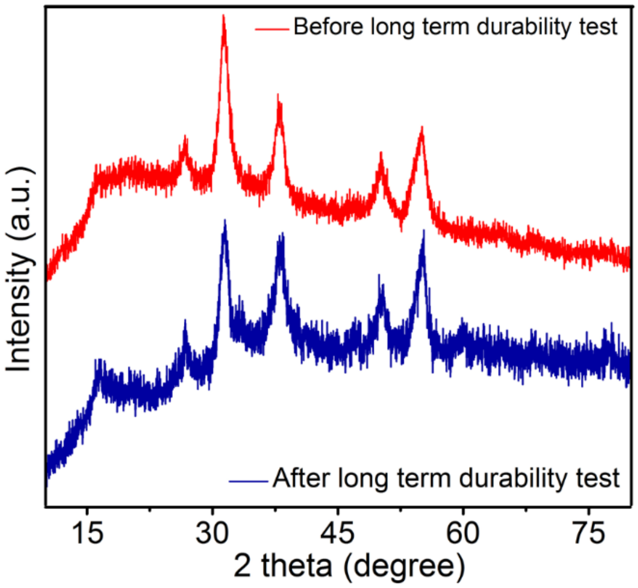

Fig. S10 XRD patterns of m-Ni_3S_4 NRs before and after long-term OER test.

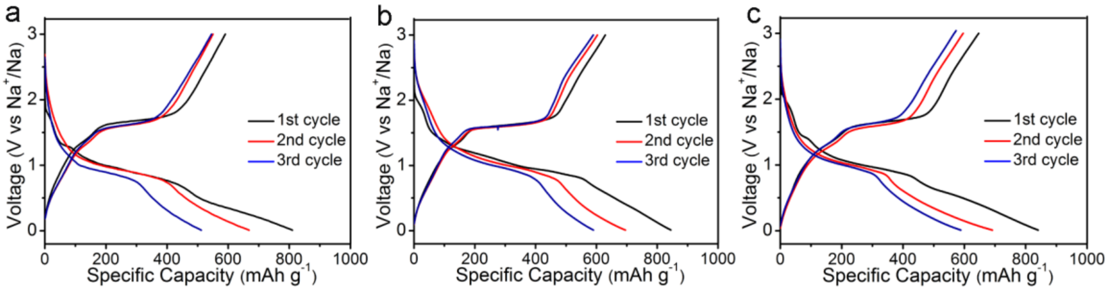

Fig. S11 Initial galvanostatic charge/discharge voltage profiles of m-Ni_3S_4 NRs/g-C_3N_4 NS (a), m-Ni_3S_4 NRs/N-G (b) hybrid and pure m-Ni_3S_4 NRs.

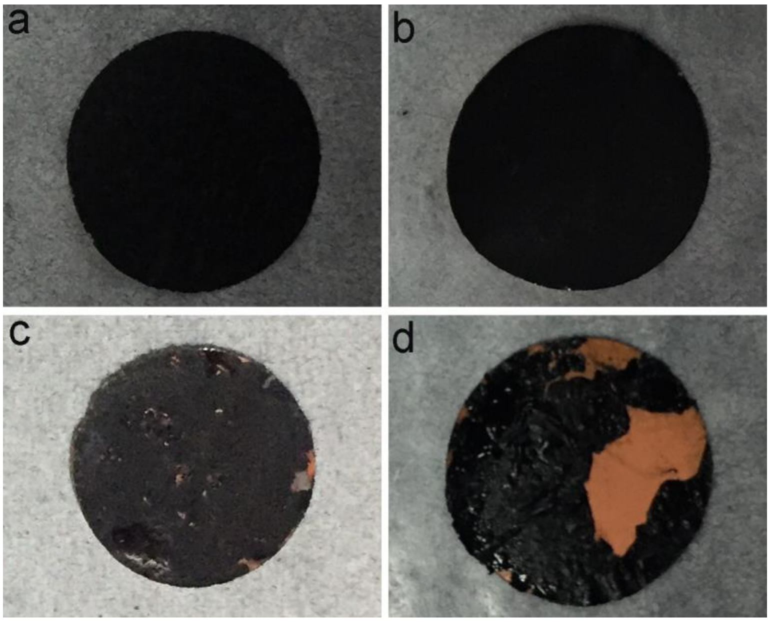

Fig. S12 The optical pictures of (a) m-Ni_3S_4 NRs/g-C_3N_4 NS/N-G ternary hybrid-, (b) m-Ni_3S_4 NRs/g-C_3N_4 NS binary hybrid-, (c) m-Ni_3S_4 NRs/N-G binary hybrid- and (d) pure m-Ni_3S_4 NRs-modified current collectors after 300th cycling performance.

Similar to electrocatalytic hydrolysis, the products of pure individuals, binary/ternary hybrids as well as corresponding mechanical mixtures were also served as sodium hosts to measure the SIB performance (the mechanical mixtures were obtained by grinding the corresponding various individual components which are in a same proportion as the hybrids based on the weight ratio detected in Table S3, Electronic Supplementary Information). The cycling performance of carbon materials were tested and depicted in Fig. S13a under a current density of 100 mA g^{-1}, the same as the measurement conditions of other Ni_3S_4-based hybrids exhibited in Fig. 7c. As detected, the discharge specific capacities for pure N-G, g-C_3N_4 NS/N-G hybrid and pure g-C_3N_4 NS are ~160 mAh g^{-1}, ~100 mAh g^{-1} and ~42 mAh g^{-1}, respectively. Thus, the contributions of carbon materials support to the specific capacities were considered to be small, while the real active specie is still m-Ni_3S_4 NRs which could be acted as a potential host for SIB especially after being modified by above substrates like g-C_3N_4 NS/N-G.

On the other hand, it is interesting to find that as for carbon materials, the pure

N-G possesses a higher specific capacity than g-C_3N_4 NS/N-G, while the pure g-C_3N_4 displays the relatively worst property for SIB. Nevertheless, after the integration with m-Ni_3S_4 NRs to form hybrids, the ternary hybrid of m-Ni_3S_4 NRs/g-C_3N_4 NS/N-G shows the greatest ability to store sodium ions among these three materials, and the cycling performance of m-Ni_3S_4 NRs/g-C_3N_4 NS is also better than that of m-Ni_3S_4 NRs/N-G. This significant change suggests that there is a synergistic effect between m-Ni_3S_4 NRs and carbon materials. In addition, the relatively excellent properties for m-Ni_3S_4 NRs/g-C_3N_4 NS/N-G and m-Ni_3S_4 NRs/g-C_3N_4 NS further reveal the important roles of carbon nitride within hybrids while in the discharge/charge processes, which mainly including promote the exposure of active sites on m-Ni_3S_4 NRs, expedite the transport of electrolyte to flood and interact with the internal active materials, stabilize the active materials to avoid agglomeration, enhance the mechanical strength as well as to release the structural stress of the hybrids through the corresponding interior void space.

Moreover, it is obvious to observe that with the progress of cyclic stability test, the pure m-Ni_3S_4 NRs and mechanical mixtures exhibit severe specific capacity degradation relative to that of corresponding hybrids. For instance, the capacities of individual m-Ni_3S_4 NRs, as well as m-Ni_3S_4 NRs + g-C_3N_4 NS, m-Ni_3S_4 NRs + g-C_3N_4 NS + N-G, m-Ni_3S_4 NRs + g-C_3N_4 NS/N-G and m-Ni_3S_4 NRs + N-G mechanical mixtures were rapidly decreased to 398, 341, 361, 390 and 443 mAh g^{-1} only after 50 cycles in a current density of 100 mA g^{-1}, respectively, while the specific capacities for the hybrids of m-Ni_3S_4 NRs/g-C_3N_4 NS, m-Ni_3S_4 NRs/g-C_3N_4 NS/N-G and m-Ni_3S_4 NRs/N-G were still kept in 590 mAh g^{-1}, 670 mAh g^{-1} and ~535 mAh g^{-1} even after 300th cycle in the same measurement conditions, respectively. Referring to the in-depth studies expounded in the article, the improvements in SIB performance of hybrids are mainly due to the synergistic effects between the components, which could really enhance the sodium ions storage properties of the active species to a great extent by retarding the anisotropic volume expansion, preventing the irreversible mechanical failure, reducing the diffusion resistance as well as accelerating the transfer speed of electrons and sodium ions during insertion/extraction process. Thus, under the above designed fair comparisons, the better cycling performance of hybrids than the corresponding pure individuals and mechanical mixtures could be certainly attributed to the existence and assist of van der Waals heterojunctions within m-Ni_3S_4 NRs/N-G, m-Ni_3S_4 NRs/g-C_3N_4 NS and m-Ni_3S_4 NRs/g-C_3N_4 NS/N-G, since there is not any other difference between them, in consistent with the conclusions obtained from the electrocatalytic activities.

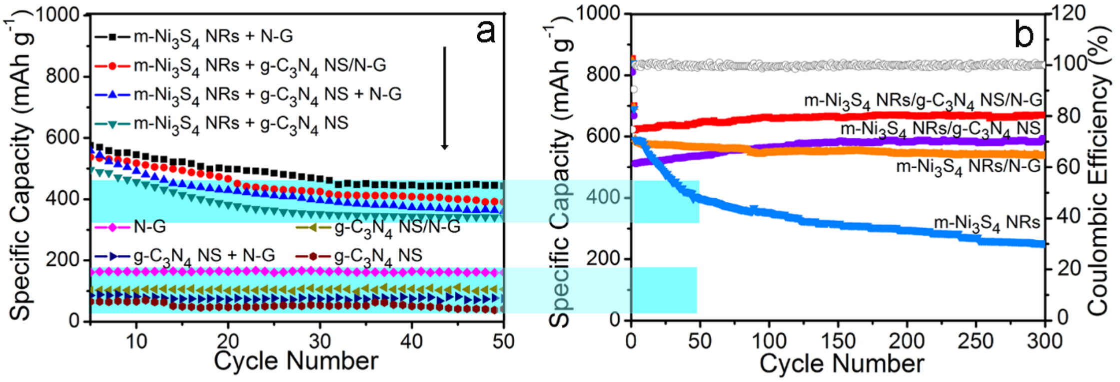

Fig. S13 (a) Cycling performance of N-G, g-C_3N_4 NS/N-G, g-C_3N_4 NS and corresponding mechanical mixtures including g-C_3N_4 NS + N-G, m-Ni_3S_4 NRs + N-G, m-Ni_3S_4 NRs + g-C_3N_4 NS/N-G, m-Ni_3S_4 NRs + g-C_3N_4 NS + N-G and m-Ni_3S_4 NRs + g-C_3N_4 NS, measured at a current density of 100 mA g^{-1}, and (b) cycling performance of m-Ni_3S_4 NRs, m-Ni_3S_4 NRs/g-C_3N_4 NS, m-Ni_3S_4 NRs/N-G and m-Ni_3S_4 NRs/g-C_3N_4 NS/N-G, measured under the same conditions as (a).

Ex-situ TEM images of m-Ni_3S_4 NRs/g-C_3N_4 NS/N-G during the repeated discharge/charge processes are displayed in Fig. S14 to confirm the outstanding cycling stability of the ternary hybrid. Compared t the TEM image before the tests of cycling stability (Fig. S14a), there are not any obvious changes on morphologies and structures for the ternary hybrid to be found after discharging/charging 300 cycles in a current density of 100 mA g^{-1}. As seen in Fig. S14b, the active species of nickel sulfide is still embedding in the carbon material of g-C_3N_4 NS/N-G matrix and almost maintaining its original nanostructures, indicating the inappreciable agglomeration, pulverization, volume expansion and mechanical failure of this electrode material during the repetitive insertion/extraction steps of SIBs. Similarly, this phenomenon could also be obviously observed in Fig. S14c which exhibits the morphology of m-Ni_3S_4 NRs/g-C_3N_4 NS/N-G even after discharging/charging 600 cycles in a higher current density of 2 A g^{-1}, further suggesting the great potential of this ternary hybrid composite developed in current work as a superior host for sodium ion storage and with an excellent mechanical stability upon long cycling. Furthermore, the *ex-situ* TEM images of m-Ni_3S_4 NRs/g-C_3N_4 NS (Fig. S14d and S14e), m-Ni_3S_4 NRs/N-G binary hybrids (Fig. S14f and S14g) and pure m-Ni_3S_4 NRs (Fig. S14h and S14i) before cycling stability tests and after charging/discharging 300 cycles in a current density of 100 mA g^{-1} were also detected, respectively. Because of the robust buffer system of g-C_3N_4 NS, the hybrid of m-Ni_3S_4 NRs/g-C_3N_4 NS reveals excellent cyclic stability performance as well, the same as m-Ni_3S_4 NRs/g-C_3N_4 NS/N-G ternary hybrid. On the contrary, after charging/discharging 300 cycles, the morphologies and structures of m-Ni_3S_4 NRs/N-G binary hybrids and pure m-Ni_3S_4 NRs show great difference compared with that before cycling stability tests, as seen in Fig. S14g and Fig. S14i, most of the active species fall off carbon substrate and the serious agglomeration of active species lead the specific capacity decayed in different degrees, consisting with the consequence obtained from part of batteries measurements in Fig. 7.

On the other hand, Fig. S14 could also explain the activation process of batteries in Fig. 7c and 7f. Actually, the activation process could be obviously observed in the cyclic stability curves of both m-Ni_3S_4 NRs/g-C_3N_4 NS and m-Ni_3S_4 NRs/g-C_3N_4 NS/N-G hybrids, it starts after the initial 3 cycles and dribbles away at around 120th cycle (as seen in Fig. 7c). As a matter of fact, this is a common phenomenon which occurs in many carbon coated materials while under the measurements of ion batteries.[11-20] In current work, the activation process is mainly caused by the generated structural defects on carbon materials and a 'pocket effect' for the hybrids, similar to some reported literatures.[11–20] In detail, as for carbon coated materials, with the increase of cycle numbers, it is ineluctable to introduce some defects into the carbon matrix due to the repetitive sodiation/desodiation steps. Particularly, these defects could enhance the insertion of far more Na ions in the hybrids, and advance the contact between Na ions and active substances, so as to increase the specific capacity of hybrids within a certain range.[12] However, because of the serious volume expansion and mechanical failure during the discharge/charge process (Fig. S14f and S14g), there is a macroscopic capacity fading for m-Ni_3S_4 NRs/N-G and it could make more effects than the newly generated structural defects on SIB performance in overall result (revealed from Fig. 7c), thus, the activation processes can be only observed in the hybrids of m-Ni_3S_4 NRs/g-C_3N_4 NS and m-Ni_3S_4 NRs/g-C_3N_4 NS/N-G rather than m-Ni_3S_4 NRs/N-G, and let alone for the pure m-Ni_3S_4 NRs without combined carbon substrate. Additionally, in spite of the stabilized structures of hybrids by the carbon materials, there is still some inevitable collapse of active species during the discharge/charge process. Fortunately, the g-C_3N_4 NS as a robust buffer system could stabilize the structure of active materials to the maximum extent, constraint the slightly crushed active materials and bundle them inside, just like a pocket with resilience. As seen in the following Fig. S14a to S14e, compared with the TEM image before cycling stability tests, the active species is still embedding in the carbon material of g-C_3N_4 NS/N-G and g-C_3N_4 NS matrix after repetitive sodiation/desodiation steps. In this regard, the inevitable collapse of active species within hybrids adversely becomes a positive factor for the capacity growth due to the increased interfaces and shortened ion diffusion path of the hosts. Thus, more Na ions can be stored on the newly created surfaces with interfacial charging, and the intensity of which is further enhanced with the decreased size of active materials.[13] As a consequence, the external expression for this 'pocket effect' is an activation process for m-Ni_3S_4 NRs/g-C_3N_4 NS and m-Ni_3S_4 NRs/g-C_3N_4 NS/N-G within the initial ~120 cycles (starts from the 4th cycle), respectively. On the contrary, as for m-Ni_3S_4 NRs NS/N-G and pure m-Ni_3S_4 NRs, the N-G nanosheets and Ketjenblack carbon (added in the ball-milling process) could hardly act as 'elastic pockets' to retard the immoderate collapse of active materials during the insertion/extraction process of SIBs. As seen in Fig. S14f to S14i, after repetitive charging and discharging, The morphologies and structures of m-Ni_3S_4 NRs/N-G binary hybrids and pure m-Ni_3S_4 NRs show great difference compared with that before cycling stability tests, most of the active species fall off carbon substrate in the hybrid and the serious agglomeration of active species also occurred in pure m-Ni_3S_4 NRs-modified current collector. Expectedly, the m-Ni_3S_4 NRs NS/N-G and pure m-Ni_3S_4 NRs cannot contact well with the current collectors and gradually fallen from them due to the serious anisotropic volume expansion and irreversible mechanical failure of the active materials as the process of sodiation/desodiation going on (Fig. S12c and S12d), which lead to the decay of specific capacities in different degrees, as seen in Fig. 7c. In short, because of the newly generated structural defects on carbon materials and a 'pocket effect' resulting from the robust g-C_3N_4 NS within the hybrids, an activation process appears in the cyclic stability curves of both m-Ni_3S_4 NRs/g-C_3N_4 NS and m-Ni_3S_4 NRs/g-C_3N_4 NS/N-G hybrids within the initial ~120 cycles (starts from the 4th cycle), respectively.

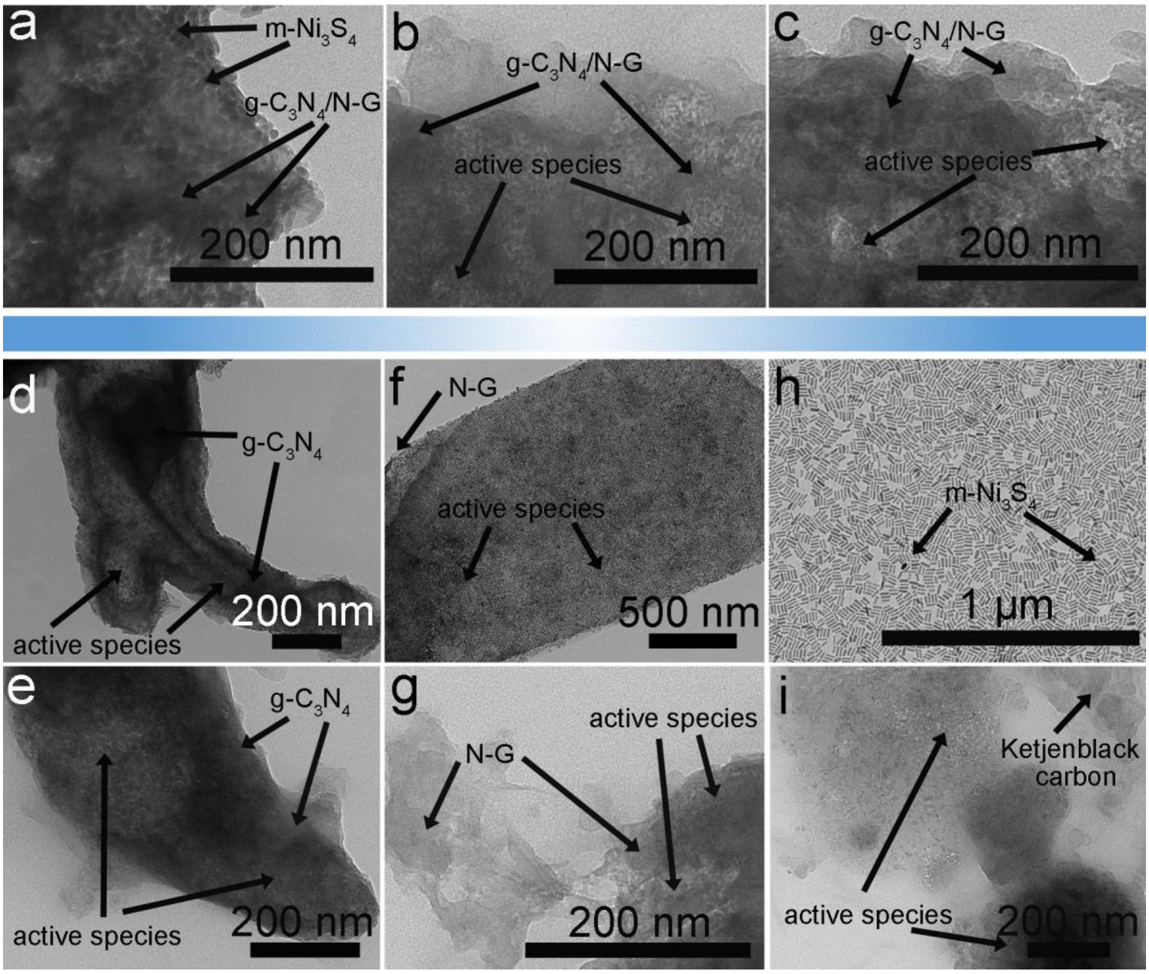

Fig. S14 TEM images of m-Ni_3S_4 NRs/g-C_3N_4 NS/N-G ternary hybrid (a) before cycling stability tests, (b) after charging/discharging 300 cycles in a current density of 100 mA g^{-1}, and (c) after charging/discharging 600 cycles in a current density of 2 A g^{-1}. TEM images of m-Ni_3S_4 NRs/g-C_3N_4 NS (d, e), m-Ni_3S_4 NRs/N-G binary hybrids (f, g) and pure m-Ni_3S_4 NRs (h, i) before cycling stability tests and after charging/discharging 300 cycles in a current density of 100 mA g^{-1}, respectively.

References

1 Y. Hou, Z. Wen, S. Cui, X. Guo and J. Chen, *Adv. Mater.,* **2013**, 25, 6291–6297.

2 N. Mahmood, C. Zhang and Y. Hou, *Small,* **2013,** 9, 1321–1328.

3 H. Li, S. Gan, H. Wang and D. Han, *Adv. Mater.* **2015**, 27, 6906–6913.

4 Y. Hou, Z. Wen, S. Cui, X. Guo and J. Chen, *Adv. Mater.*, **2013***,* 25, 6291–6297.

5 Z. Fang, Y. Wang, Y. Zou, Z. Hao and Q. Dong, *Inorg. Chem. Commun.,* **2017**, 79, 1–4.

6 P. Luo, H. Zhang, L. Liu, Y. Zhang, J. Deng, C. Xu, N. Hu and Y. Wang, *ACS Appl. Mater. Interfaces,* **2017**, 9, 2500–2508.

7 N. Jiang, Q. Tang, M. Sheng, B. You, D. Jiang and Y. Sun, *Catal. Sci. Technol.,* **2016**, 6, 1077–1084.

8 K. Jayaramulu, J. Masa, O. Tomanec, D. Peeters, V. Ranc, A. Schneemann, R. Zboril, W. Schuhmann and R. A. Fischer, *Adv. Funct. Mater.,* **2017**, 27, 1700451.

9 J.-T. Ren and Z.-Y. Yuan, *ACS Sustainable Chem. Eng.,* **2017**, 5, 7203–7210.

10J.-J. Lv, J. Zhao, H. Fang, L.-P. Jiang, L.-L. Li, J. Ma and J.-J. Zhu, *Small*, **2017**, 13, 1700264.

11 X. Li, Y. Feng, M. Li, W. Li, H. Wei and D. Song, *Adv. Funct. Mater.* **2015,** 25, 6858–6866.

12 Y. Pan, X. Cheng, L. Gong, L. Shi, T. Zhou, Y. Deng and H. Zhang, *ACS Appl. Mater. Interfaces* **2018**, 10, 31441–31451.

13 X. Jin, H. Huang, A. Wu, S. Gao, M. Lei, J. Zhao, X. Gao and G. Cao, *ACS Nano* **2018**, 12, 8037–8047.

14 X. Hong, J. Jin, T. Wu, Y. Lu, S. Zhang, C. Chen and Z. Wen, *J. Mater. Chem. A,* **2017**, 5, 14775–14782.

15 Y. Wang, X. Guo, Z. Wang, M. Lü, B. Wu, Y. Wang, C. Yan, A. Yuan and H. Yang, *J. Mater. Chem. A,* **2017**, 5, 25562–25573.

16 J. Lv, D. Bai, L. Yang, Y. Guo, H. Yan and S. Xu, *Chem. Commun.*, **2018**, 54, 8909–8912.

17 C. Yan, X. Gu, L. Zhang, Y. Wang, L. Yan, D. Liu, L. Li, P. Dai and X. Zhao, *J. Mater. Chem. A,* **2018**, 6, 17371–17377.

18 N. Voronina, H. Yashiro and S.-T. Myung, *J. Mater. Chem. A,* **2018,** 6, 17111–17119.

19 G. K. Veerasubramani, Y. Subramanian, M.-S. Park, G. Nagaraju, B. Senthilkumar, Y.-S. Lee and D.-W. Kim, *J. Mater. Chem. A*, **2018**, 6, 20056–20068;

20 R. Zou, M. Xu, S.-A. He, X. Han, R. Lin, Z. Cui, G. He, D. J. L. Brett, Z. X. Guo, J. Hu and I. P. Parkin, *J. Mater. Chem. A,* **2018**, 6, 19853–19862.